SANDIA REPORT

SAND2024-13558
Printed September 2024

Journey to Time-Variable Moment Tensors through Inversion of Acoustic and Seismoacoustic Data

Elizabeth Berg, Andréa Darrh, & Leiph Preston

Prepared by
Sandia National Laboratories
Albuquerque, New Mexico 87185
Livermore, California 94550

Issued by Sandia National Laboratories, operated for the United States Department of Energy by National Technology & Engineering Solutions of Sandia, LLC.

Available to DOE and DOE contractors from

U.S. Department of Energy
Office of Scientific and Technical Information
P.O. Box 62
Oak Ridge, TN 37831

Telephone: (865) 576-8401
Facsimile: (865) 576-5728
E-Mail: reports@osti.gov
Online ordering: http://www.osti.gov/scitech

Available to the public from

U.S. Department of Commerce
National Technical Information Service
5301 Shawnee Road
Alexandria, VA 22312

Telephone: (800) 553-6847
Facsimile: (703) 605-6900
E-Mail: orders@ntis.gov
Online order: https://classic.ntis.gov/help/order-methods

ABSTRACT

We explore the capability of acoustic and seismoacoustic datasets to directly resolve a complex, time-variable source consisting of a buried mechanism, represented as a moment tensor, and a spall mechanism, represented as a vertical force at the surface. Traditionally, each component of a resolved moment tensor assumes one underlying source time function, which likely fails to capture the full evolution of a dynamic source, such as an explosion followed by slip on near-source joints or development of spallation. Specifically, we expand previous work to resolve a time-variable moment tensor using single-modality and joint-modality inversion frameworks through analysis of infrasound and seismoacoustic data recorded as part of the Source Physics Experiment Phase II: Dry Alluvium Geology (DAG). We investigate the impact of including signals from seismic-to-air coupling that are local to each infrasound sensor in comparison to mainly atmosphere-propagating acoustic signals, which occur from coupling of the wavefield from the subsurface to the atmosphere directly above the source. Additionally, we assess the ability of our inversion algorithm to fit observed infrasound data using a variety of time-variable source mechanisms. First, we consider the buried moment tensor source alone, which assumes that the determined Green's functions incorporate effects from spallation or that the impact from spallation is minimal. Second, we examine the estimated buried moment tensor and vertical surface spallation as terms that must both be resolved in the inversion. Third, we assess the ability for an estimated vertical surface spallation source to fit the acoustic data on its own. Finally, we compare results from the joint inversion of both seismic geophone and infrasound acoustic data for the buried-only source compared to buried and spallation sources. Our results are a preliminary investigation into the applications of the inversion technique to recorded datasets and show the technique has limited capabilities using acoustic data alone. Instead, this method shows promise for seismic and seismoacoustic datasets to resolve the time-variable mechanisms of a buried source.

ACKNOWLEDGMENT

This Source Physics Experiment (SPE) research was funded by the National Nuclear Security Administration, Defense Nuclear Nonproliferation Research and Development (NNSA DNN R&D). The authors acknowledge important interdisciplinary collaboration with scientists and engineers from LANL, LLNL, NNSS, and SNL We also thank Christian Poppeliers for being instrumental in the foundation and continuation of this research. Additionally, we thank Marlon Ramos for his invaluable technical review of this report, which has been instrumental in ensuring readiness for release. Sandia National Laboratories is a multimission laboratory managed and operated by National Technology & Engineering Solutions of Sandia, LLC, a wholly owned subsidiary of Honeywell International Inc., for the U.S. Department of Energy's National Nuclear Security Administration under contract DE-NA0003525.

CONTENTS

LIST OF FIGURES

1. INTRODUCTION

Buried explosion sources can often be challenging to accurately characterize, with complex wavefields that can have a significant amount of shear wave energy (Kisslinger et al., 1961; Wright and Carpenter, 1962), despite an explosion being assumed to be an isotropic, compressive source in theory. There are four main mechanisms that can occur in the near-source region that can cause an explosive source to appear more akin to an earthquake, including 1) explosion-generated spall, where the ground is upheaved and falls back to the surface, resulting in the generation of vertically polarized shear waves and Rayleigh waves (Day et al., 1983; Day and McLaughlin, 1991), 2) slip on near-source joints or pre-existing faults (Wallace et al., 1983; Day et al., 1987; Stevens and Thompson, 2015), 3) non-sphericity of the source causing the conversion of P and Rayleigh waves into S-waves (Baker et al., 2012a,b), and 4) scattering (Stevens et al., 2004; Patton and Taylor, 1995). Categorizing both the influence of spall on the seismoacoustic wavefield and any near-source joint slippage is therefore necessary to accurately characterize a buried explosion source.

A seismic source is generally represented by the mechanical energy the source releases into the Earth. This mechanical energy is often portrayed using time-invariant moment tensors which only portray a single source mechanism for the energy output into the Earth. Common practice for modeling these moment tensors is to describe the source energy using identical source time functions (STFs) for all components of the moment tensor, decided based on the anticipated source type (e.g. Chiang et al., 2016; Ford et al., 2009; Herrmann et al., 2011; Rösler and Stein, 2022). This means more complex sources that evolve with time, such as an explosion followed by near-source joint slip, are not considered unless explicitly defined. However, inversions that use time-variable moment tensors with independent STFs can capture the time evolution of these more complex sources (e.g. Poppeliers et al., 2018; Poppeliers and Preston, 2020, 2021, 2022b; Berg and Poppeliers, 2022a).

Following a similar implementation as in Berg and Poppeliers (2022a), we apply our time-variable moment tensor inversion to recorded infrasound and seismic geophone data from the Source Physics Experiment (SPE) Phase II: Dry Alluvium Geology (DAG), specifically the DAG-4 experiment. We invert the infrasound data recorded by microbarometers for the 6 moment tensor components and vertical force function, focused on the acoustic wavefield. While the recorded infrasound data may also contain local infrasound, earth-traveling pressure waves that couple to the atmosphere at the infrasound sensor, we instead focus on the acoustic wavefield that propagates mainly through the atmosphere. Additionally, we investigate the source mechanisms resolved from jointly inverting seismoacoustic data. We evaluate these inversions for the entire infrasound data, including coupled seismic to atmosphere signals at each station, as well as for data windowed around the typical acoustic signals that traveled through the atmosphere directly to the station. We represent our results as both time-variable moment tensor functions as well as plot these results on a fundamental lune (Tape and Tape, 2012, 2013) to visualize the time evolution of the source.

2. METHODOLOGY

We focus on applying a time-variable moment tensor and vertical force function inversion to acoustic and seismoacoustic data collected from the DAG-4 experiment. The infrasound data have significant influence from ground motion due to seismic wave arrivals (Figure 2-1), and therefore we test our inversion with both the full infrasound data as well as data windowed around the anticipated air wave arrival to see the effect that these pre-acoustic signals have on our inversion. This windowing is accomplished by first using local weather station sonde data, including humidity and temperature, to estimate the air soundspeed at the time of the DAG-4 experiment, which is determined to be approximately 347 m/s. The infrasound data are then demeaned and detrended with a 50% Tukey window of length 2.25 seconds applied around the anticipated acoustic arrival time. The seismic data are more numerous than the infrasound data, so a few approaches with differing seismic station selections in our seismoacoustic inversions are shown. Both the infrasound and seismic data are resampled to 50 samples/sec in all inversions and filtered to a frequency band of 0.5 to 4 Hz using a 6th order Chebyshev bandpass filter.

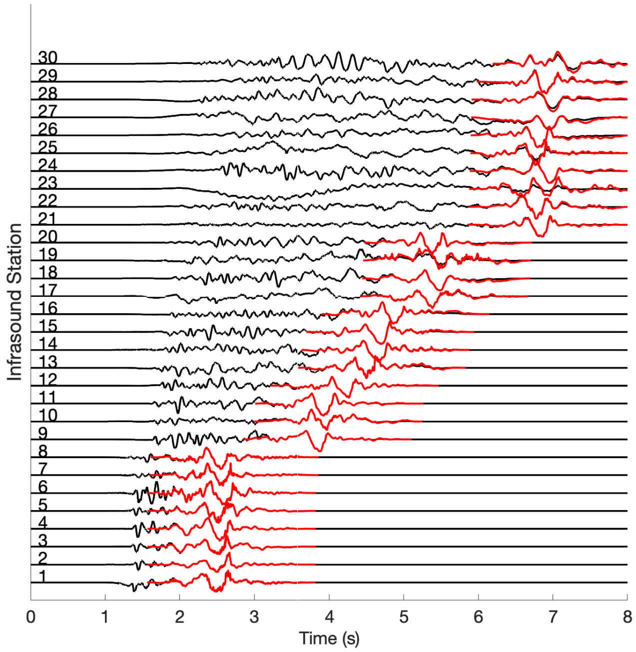

Figure 2-1 Signals recorded by microbarometers stationed around the source, as shown in Figure 3-1, relative to the DAG-4 origin time. These signals include both acoustic-only arrivals (red) and seismic-to-air coupled arrivals (black).

2.1. Components of the inversion

Within this study, we improve upon the previously developed time-variable moment tensor algorithm defined in Berg and Poppeliers (2022a). We first define the far-field seismic wavefield in the time domain (Aki and Richards, 2002) assuming that the source region is a point source

$$d_k(\mathbf{x}', t') = \sum_{l=1}^{L} \int_{-\infty}^{\infty} g_{k,l}(\mathbf{x}', t; \mathbf{x}, t) m_l(\mathbf{x}, t) dt \tag{1}$$

where d_k is the particle velocity at station k located at an observation point $\mathbf{x}' = [x', y', z']$, $g_{k,l}$ describe the Green's functions at the l^{th} source component, and m_l are the series of time-varying forces and/or force couples acting at the source location, $\mathbf{x}$, of which there are L in total. We can simplify equation 1 to the linear forward problem

$$\mathbf{d} = \mathbf{Gm}, \tag{2}$$

where $\mathbf{d}$ is a vector of length N containing the infrasound or seismoacoustic data time series at all stations, $\mathbf{G}$ are the Green's functions matrix of size NxM, and $\mathbf{m}$ is the model vector of length M comprised of the six unique time-variable moment tensor M_{ij} rate functions as well as a vertical force function F_z.

Further defining equation 2 we have the following relation

$$\begin{bmatrix} d_1(t) \\ d_2(t) \\ d_3(t) \\ \vdots \\ d_K(t) \end{bmatrix} = \begin{bmatrix} [\mathbf{G}_{1,1}] & [\mathbf{G}_{1,2}] & \cdots & [\mathbf{G}_{1,L}] \\ [\mathbf{G}_{2,1}] & [\mathbf{G}_{2,2}] & \cdots & [\mathbf{G}_{2,L}] \\ [\mathbf{G}_{3,1}] & [\mathbf{G}_{3,2}] & \cdots & [\mathbf{G}_{3,L}] \\ \vdots & \vdots & \ddots & \vdots \\ [\mathbf{G}_{K,1}] & [\mathbf{G}_{K,2}] & \cdots & [\mathbf{G}_{K,L}] \end{bmatrix} \begin{bmatrix} M_1(t) \\ M_2(t) \\ M_3(t) \\ \vdots \\ M_L(t) \end{bmatrix}, \tag{3}$$

where each $\mathbf{G}_{k,l}$ matrix corresponding to the k^{th} station and l^{th} moment tensor component or spall term is

$$\mathbf{G}_{k,l} = \begin{bmatrix} \mathbf{G}_{k,n}(t_1) & 0 & \cdots & 0 & 0 \\ \mathbf{G}_{k,n}(t_2) & \mathbf{G}_{k,n}(t_1) & 0 & \cdots & 0 \\ \mathbf{G}_{k,n}(t_3) & \mathbf{G}_{k,n}(t_2) & \mathbf{G}_{k,n}(t_1) & 0 & \vdots \\ \vdots & \vdots & \ddots & \ddots & 0 \\ \mathbf{G}_{k,n}(t_T) & \mathbf{G}_{k,n}(t_{T-1}) & \cdots & \mathbf{G}_{k,n}(t_2) & \mathbf{G}_{k,n}(t_1) \end{bmatrix}, \tag{4}$$

where $\mathbf{G}_{k,l}$ is a TxT discrete convolution matrix and T is the total number of samples in time of each waveform. With this formulation, there is an inherent assumption that there is no information past time sample T. In the seismoacoustic formulation, the seismic Green's functions associated with a given moment tensor component or spall term are also included above the infrasound Green's functions when building matrix G.

$$\begin{bmatrix} d_1(t) \\ \vdots \\ d_{K_{seis}}(t) \\ d_1(t) \\ \vdots \\ d_{K_{infra}}(t) \end{bmatrix} = \begin{bmatrix} [\mathbf{G}_{seis(1,1)}] & [\mathbf{G}_{seis(1,2)}] & \cdots & [\mathbf{G}_{seis(1,L)}] \\ \vdots & \vdots & \ddots & \vdots \\ [\mathbf{G}_{seis(K_{seis},1)}] & [\mathbf{G}_{seis((K_{seis},2)}] & \cdots & [\mathbf{G}_{seis(K_{seis},L)}] \\ [\mathbf{G}_{infra(1,1)}] & [\mathbf{G}_{infra(1,2)}] & \cdots & [\mathbf{G}_{infra(1,L)}] \\ \vdots & \vdots & \ddots & \vdots \\ [\mathbf{G}_{infra(K_{infra},1)}] & [\mathbf{G}_{infra(K_{infra},2)}] & \cdots & [\mathbf{G}_{infra(K_{infra},L)}] \end{bmatrix} \begin{bmatrix} M_1(t) \\ M_2(t) \\ M_3(t) \\ \vdots \\ M_L(t) \end{bmatrix}, \tag{5}$$

where $G_{seis}(k,l)$ are the seismic Green's functions associated with the k^{th} seismic station and l^{th} moment tensor component or spall term, G_{infra} are the acoustic Green's functions associated with the k^{th} infrasound station and l^{th} moment tensor component or spall term, and K_{seis} and K_{infra} are the total seismic and infrasound stations, respectively.

We generate Green's functions for all stations through Parelasti, a 3D finite difference solution to the elastic wave equation (Poppeliers and Preston, 2021). These Green's functions are generated using a model with a spatial discretization of 5m that are built using layers and velocities from the geologic framework model (GFM) (Prothro and Wagoner, 2020) for the region and alluvium velocity values from Vieceli et al. (2022). This discretization allows for predicted data with a maximum frequency of ~7.5 Hz before encountering numerical dispersion. We filter the acoustic and seismoacoustic data we use in our inversions to a frequency band where we anticipate and observe the majority of the infrasound signal to be in: 0.5 to 4 Hz.

The infrasound Green's functions are aligned with the data by filtering both the data and the sum of the diagonal moment tensor Green's functions to the same frequency band using a 6th order Chebyshev filter and cross-correlating. The time lags between the filtered observed data and Green's functions are then measured from the highest correlation, and used to align the infrasound Green's functions to the observed data. The Green's functions are not filtered in the actual inversion, only the time lags from the above process are used to shift the Green's function arrivals to match the observed data arrival times.

The seismic Green's functions, on the other hand, are aligned through the use of a standard STA/LTA algorithm. We use this algorithm to pick the first arrivals of the unfiltered observed data and unfiltered sum of the vertical component diagonal moment tensor Green's functions, and then used these picks to shift all Green's functions to the same arrival time as the observed data.

2.2. Inversion formulation

The linear parametric inversion is therefore defined using a least squares regularization, more specifically a Tikhonov regularization formulation. We first minimize an objective function

$$\min \phi = \phi_d + \xi \phi_m, \tag{6}$$

where ϕ is the objective function being minimized and ϕ_d and ϕ_m are the data misfit objective function and model objective function respectively. In this inversion, we define the data objective function as a simple, squared L_2 norm misfit between the observed ($\mathbf{d_{obs}}$) and predicted data ($\mathbf{d_{pre}}$)

$$\phi_d = ||\mathbf{d_{obs}} - \mathbf{d_{pre}}||^2. \tag{7}$$

The model objective function is defined as a combination of smallest and 2nd order smoothest model norms

$$\phi_m = \alpha \int \mathbf{m}^2 dt + \beta \int \left(\frac{d^2\mathbf{m}}{dt^2} \right)^2 dt \tag{8}$$

where t is time, α is the smallest model weighting parameter, and β is the smoothest model weighting parameter. The second order derivative in equation 8 can be represented by a matrix L

$$L = \begin{pmatrix} 1 & -2 & 1 & 0 & \cdots \\ 0 & \ddots & \ddots & \ddots & \\ 0 & \cdots & 1 & -2 & 1 \end{pmatrix}, \tag{9}$$

when the model is multiplied by L, this therefore results in a finite difference approximation of the second derivative. L is staggered at the length of each moment tensor component within **m** to avoid smoothing the first values of one moment tensor or vertical force function component with the last values of the previous moment tensor component in the model vector. The model objective function can then be represented as a squared L_2 norm

$$\phi_m = ||\mathbf{W_m m}||^2 \tag{10}$$

where $\mathbf{W_m}^T\mathbf{W_m}$ is equal to $\mathbf{W_m}^T\mathbf{W_m} = \alpha\mathbf{I} + \beta\mathbf{L}^T\mathbf{L}$. Taking the derivative of equation 6 with respect to **m** results in the solution

$$\mathbf{m} = (\mathbf{G}^T\mathbf{G} + \xi\mathbf{W_m}^T\mathbf{W_m})^{-1}\mathbf{G}^T\mathbf{d_{obs}}, \tag{11}$$

where ξ is a Lagrange parameter that balances the weight between the data and model objective functions. In order to find ξ we solve equation 11 for a range of ξ and use the L-curve criterion to select our final ξ value. Specifically, the final Lagrange parameter was selected as the value that resulted in ϕ_m and ϕ_d values at the maximum point of curvature on the Tikhonov curve according to the L-curve criterion.

2.3. Fundamental lune

Following Berg and Poppeliers (2022a), we represent our inversion results on a fundamental lune to better characterize how a source evolves through time. A fundamental lune is a visualization tool that allows for the identification of the source mechanism at a given point in time along the six unique moment tensor components. Source type plots were originally introduced by Hudson et al. (1989), with the fundamental lune representation introduced by Tape and Tape (2012).

The fundamental lune source-type plot is constructed through finding the eigenvalues Λ of the moment tensor M through eigen decomposition

$$M = U\Lambda U^{-1}, \tag{12}$$

where U are the eigenvectors. The eigenvalues, Λ are represented as

$$L = \begin{bmatrix} \lambda_1 & 0 & 0 \\ 0 & \lambda_2 & 0 \\ 0 & 0 & \lambda_3 \end{bmatrix} \tag{13}$$

and determine the size and pattern of a beachball representation of a focal mechanism.These eigenvalues are plotted on a portion of the unit sphere $\mathbb{W}$, with coordinates of longitude (γ)

$$\tan(\gamma) = \frac{-\lambda_1 + 2\lambda_2 - \lambda_3}{\sqrt{3}(\lambda_1 - \lambda_3)}, \tag{14}$$

and latitude $\delta = \pi/2 - \beta$, where β is the colatitude

$$\cos(\beta) = \frac{\lambda_1 + \lambda_2 + \lambda_3}{\sqrt{3}||\Lambda||}, \tag{15}$$

and $||\Lambda||$ is the L_2 norm of Λ. We restrict the location of the γ and δ on the unit sphere by enforcing ordering of the eigenvalues to be $\lambda_1 \geq \lambda_2 \geq \lambda_3$. This then results in longitude (γ) having a potential range of $-\pi/6$ to $\pi/6$ and latitude (δ) ranging from $-\pi/2$ to $\pi/2$, the latitude locations of an implosion or explosion, respectively.

3. RESULTS

We use the entirety of the infrasound station data (Figure 3-1a) for our acoustic inversions, as well as a subsection of the infrasound and seismic stations for our seismoacoustic inversions (Figure 3-1b).

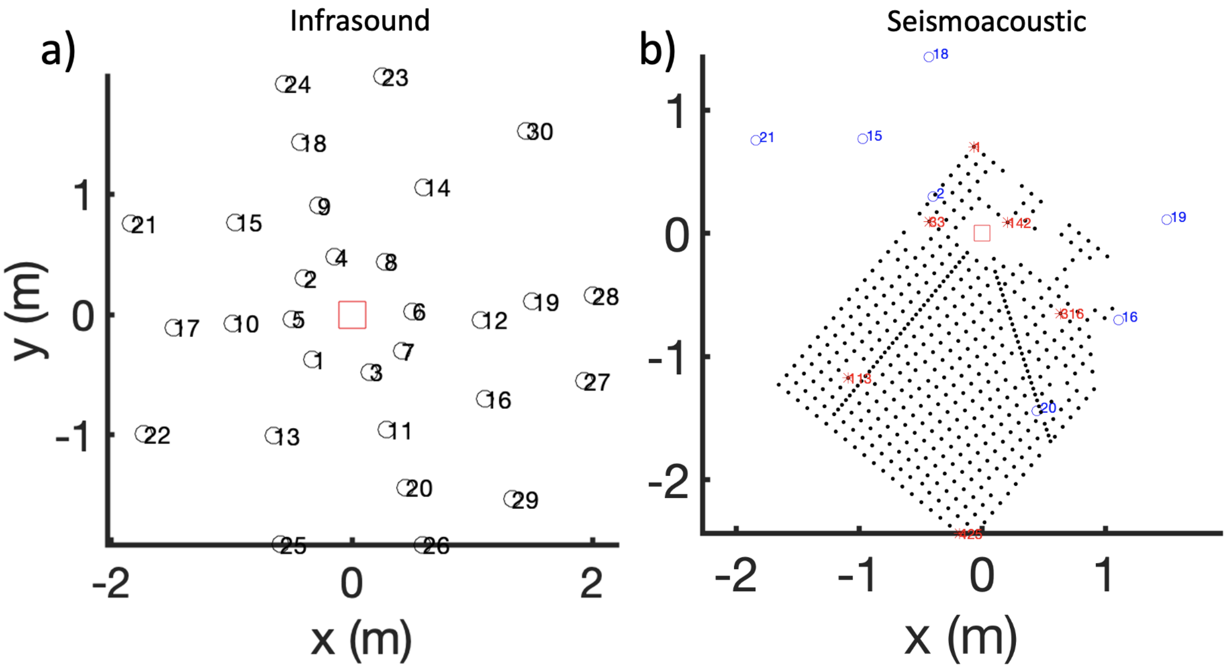

Figure 3-1 Map surrounding surface ground zero (red square) of (a) Hyperion infrasound stations (black circles, labeled by station number) used in inversions of infrasound-only data. Similarly, (b) contains the map of stations used in the inversions of seismic and infrasound data. All seismic nodal stations are shown as black dots while red stars indicate those used in the inversion. Blue circles show infrasound stations used in the seismoacoustic inversions.

For the acoustic inversions, we invert only infrasound signals corresponding to the acoustic arrivals (see Figure 2-1). We conduct inversions with and without resolving the vertical surface spall source, Fz, as well as the investigate Fz as the sole source. The inversion that does not invert for Fz returns the six unique moment tensor components, estimating the source mechanism to be solely related to the buried seismic source. We repeat this with the seismoacoustic inversions, adding in the seismic data for a variety of stations located in the Large-*N* array with different azimuths and offsets (see Figure 3-1).

3.1. Infrasound inversions

We investigate our time-variable inversion by only retaining the acoustic signals, windowing to remove the seismic-to-atmosphere coupled signals while retaining the full record length, recorded by the microbarometers surrounding DAG-4. To ensure we focus solely on the acoustic signals and corresponding information estimated in the Green's Functions, we window the Green's functions and data to only include the acoustic signal, rather than preserving the entire record, as the Green's functions are already aligned to the data. Additionally, we incorporate weighting to tamp wrap-around effects in the latter resolved portion of the resolved source-time functions (STFs) following inversion of the Green's functions and infrasound data. We use these tamped, realistic portions of the STFs to predict the data.

We first invert the acoustic data for the six unique moment tensor components, M_{xx}, M_{yy}, M_{zz}, M_{xy}, M_{xz}, and M_{yz}, as shown in Figure 3-2, such that our estimated source mechanism is solely related to the buried seismic source and does not include the vertical surface spall source. As shown in Figure 3-2a, we have strong fit to the data at stations near and far from the source. We also show both the traditionally used STF in terms of moment (see Figure 3-2b) and what we directly estimate in our inversion, the moment rate functions of Mij (see Figure 3-2c). However, we do note that our incorporated taper to the estimated STFs does result in the high-frequency effect in the predicted time-series, which can be seen around 6 s for station 4 (Figure 3-2). To accurately estimate variance reduction, we only assess the windowed portion of the observed and corresponding predicted data, which limits the impact of ringing effect to our assessment of the estimated STFs. For the inversion to determine the buried source, Mij, using acoustic data, we obtain a variance reduction of 59.5% and a correlation coefficient of 0.81. When we incorporate resolving the Fz STF into our inversion, the vertical estimate of the surface spall with the positive direction corresponding to an upward-directed force, we see that the late time ringing effect in the predicted time-series becomes more pronounced, likely due to tapering the Fz after 3.5 s (see Figure 3-3). Similarly to the Mij only result, we are able to fit the data at both near and far stations from the source, and have an increased variance reduction of 69.9% and correlation coefficient of 0.88 between the observed and predicted data. To assess how accurately the Fz term alone can resolve the observed data, we show the inversion results with only this term in Figure 3-4, which shows that the term alone can completely resolve the acoustic signals. The variance reduction is 47% and correlation coefficient is 0.74 between the observed and predicted data using the determined Fz. We show the estimated Mij STFs on a lune (see Figure 3-5) and in terms of decomposition into isotropic, CLVD, and double-couple contributions. In Figure 3-5a, we see the inversion resolving solely Mij contains mainly isotropic energy associated with a collapse, followed by cracking and linear vector dipole contributions. Figure 3-5b shows the results for the inversion resolving both Mij and Fz, which has a strong isotropic explosion signal followed by cracking, compensated linear vector dipole, and double-couple contributions. However, the STF decomposition for both results do not follow a typical trend for explosion sources (e.g., Haskell,

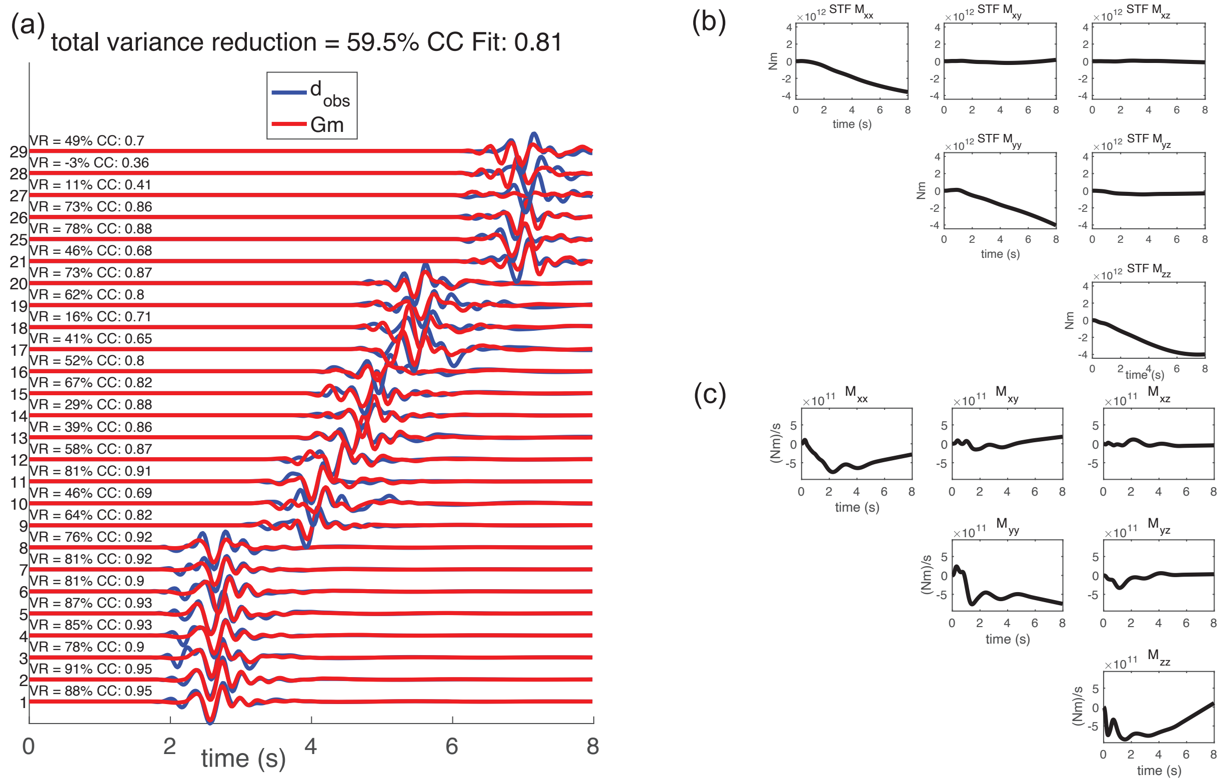

Figure 3-2 (a) Observed (blue) and predicted (red) infrasound data from inversion of acoustic signals. Title value represents average variance reduction (VR) and correlation coefficient (CC), which are specified for each station within the plot. (b) Source-time moment functions of the buried seismic source. (c) Source-time moment rate functions of the buried seismic source, which are directly estimated in the inversion.

1967). Typically, this curve begins near 0, and then increases exponentially to a maximum peak, which is a slight overshoot, and falls slightly to a flat moment value.

3.2. Seismoacoustic inversions

We next invert seismic data alongside our infrasound data in a joint inversion formulation. We use a subsection of the infrasound and seismic stations in the joint inversion, displayed in Figure 3-1, including data from seven infrasound sensors and six seismic three-component sensors. For the seismic data included in the inversion, we use the full waveform, but we limit the infrasound data to the acoustic-only arrival data.

Incorporating the seismic data along with the full infrasound data (Figure 3-6), the overall data fit drops, with the highest variance reduction at -40% for the seismic results and 87% for the infrasound, with similarly high correlation coefficients for infrasound data and low for seismic. However, while the moment tensor results in Figure 3-6b have simpler, less oscillatory behavior, we cannot fully interpret these results due to the fact that this behavior is more likely due to the inversion underfitting the observed data. This underfitting results in low frequency behavior in the moment tensor results that would not be the case if the joint inversion was able to fit the data better.

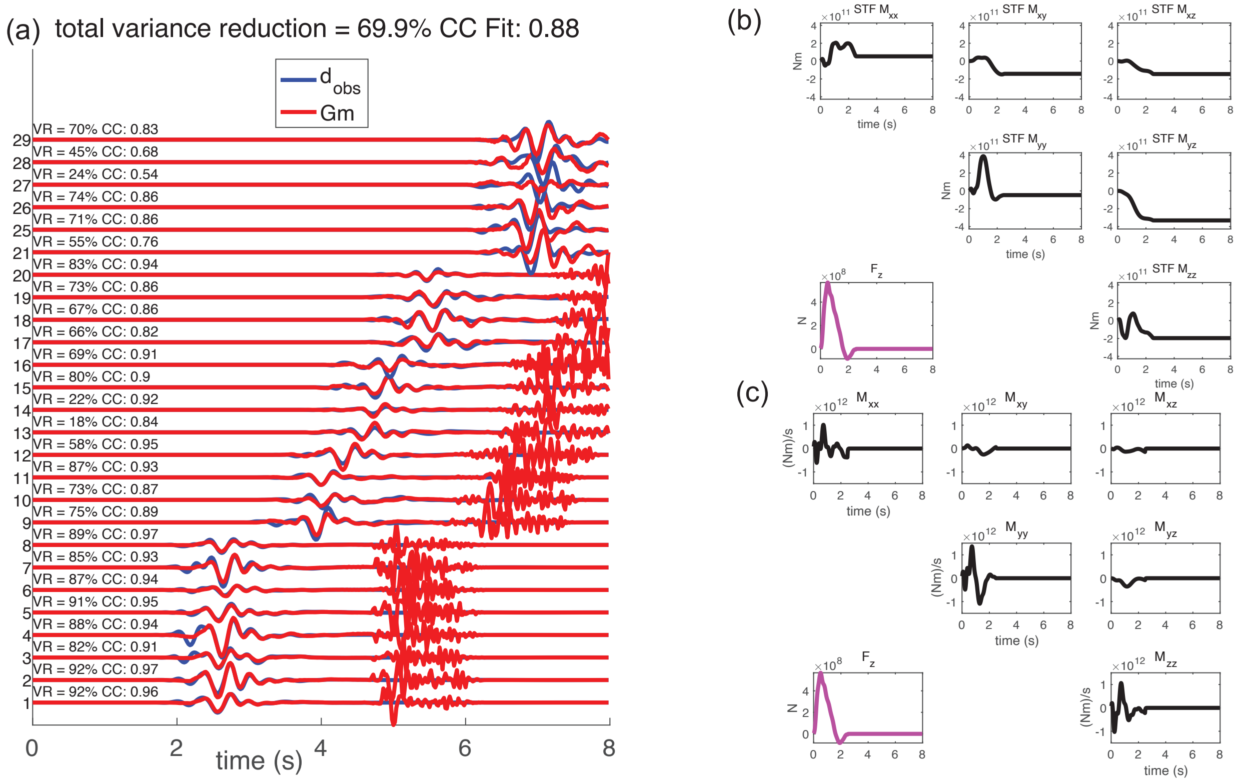

Figure 3-3 Similar to Figure 3-2, except that our inversion estimates both buried seismic source (Mij) and spallation (Fz) source-time moment rate functions.

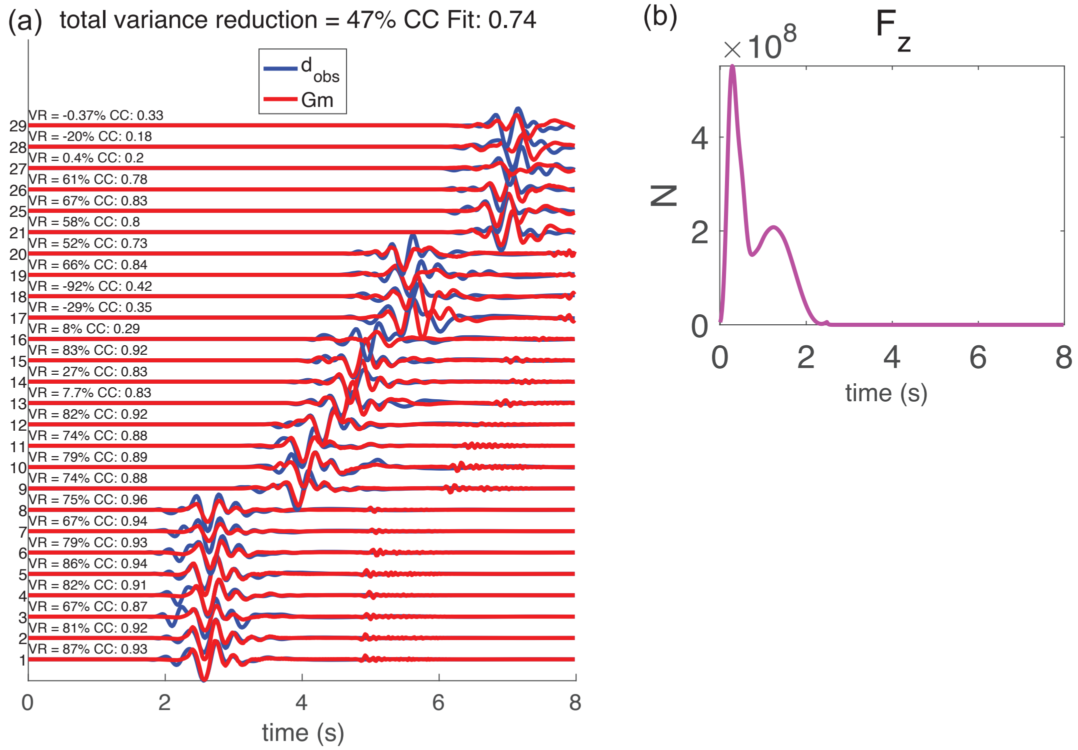

Figure 3-4 Similar to Figure 3-2, except that the estimated source moment rate functions include only the Fz spallation term.

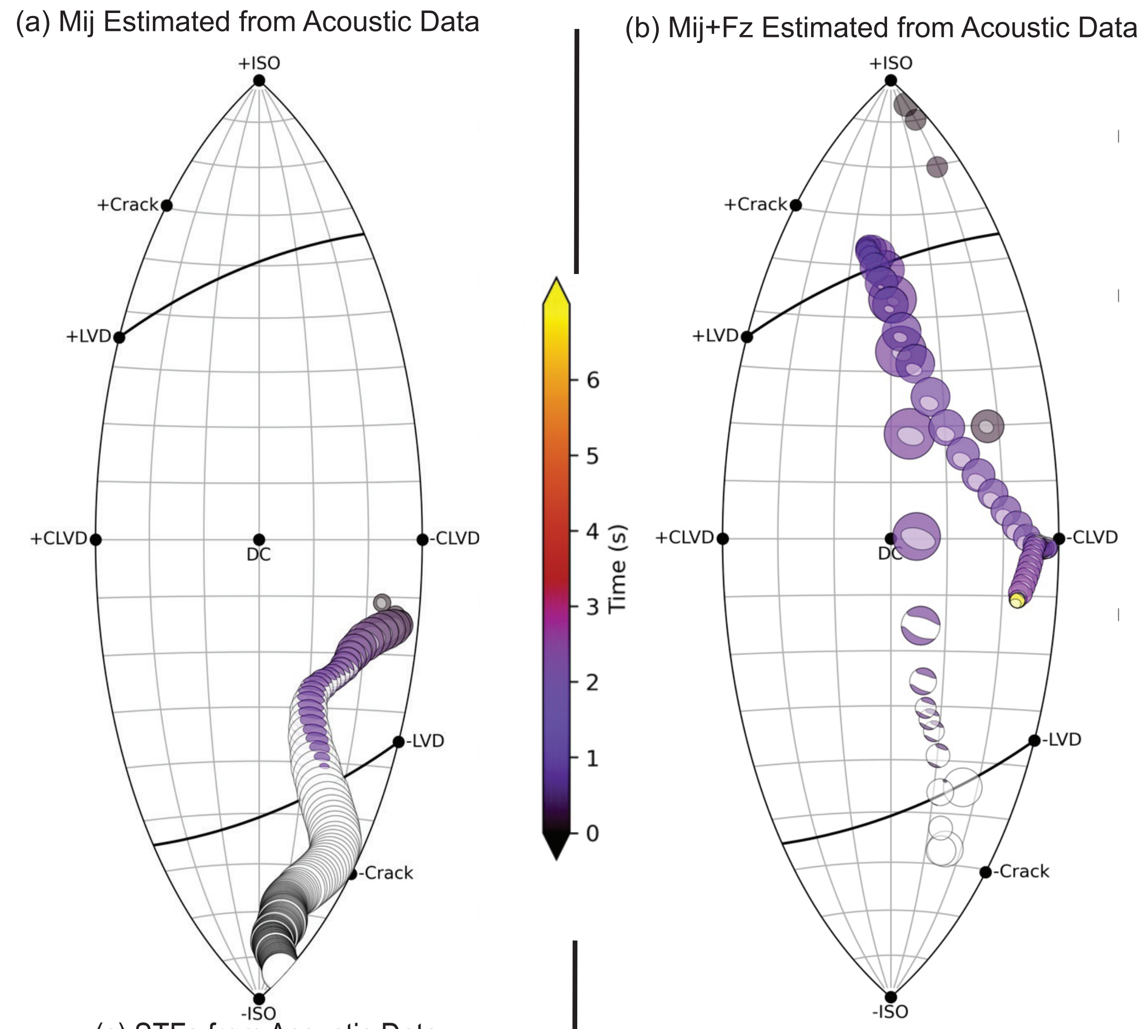

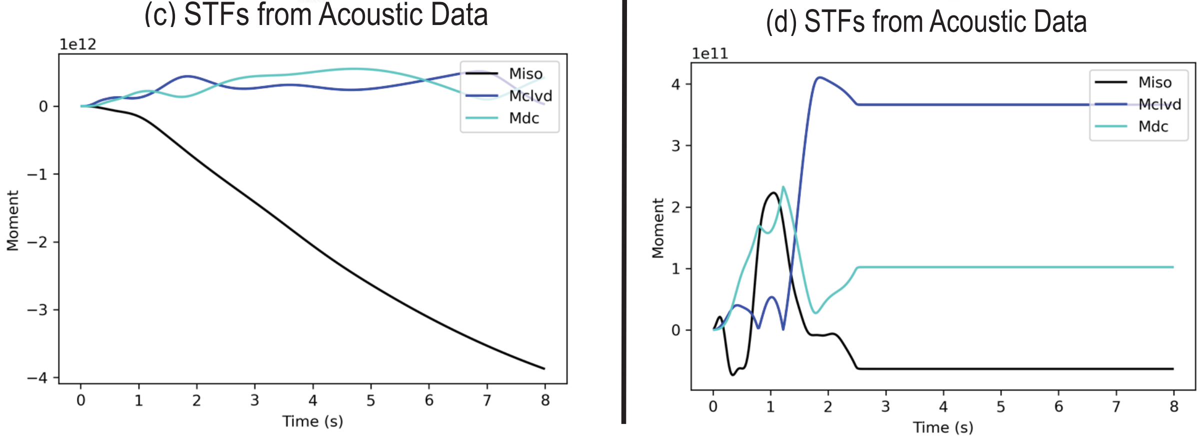

Figure 3-5 Lune visualization of the estimated buried source moment rate functions using (a) acoustic data to resolve Mij alone as compared to (b) acoustic signals to resolve Mij and Fz STFs. (c) Decomposition of Mij in terms of compensated linear vector dipole (CLVD), double couple (DC), and isotropic (ISO) STFs. (d) Similar to (c), but for Mij when Fz is incorporated into the inversion.

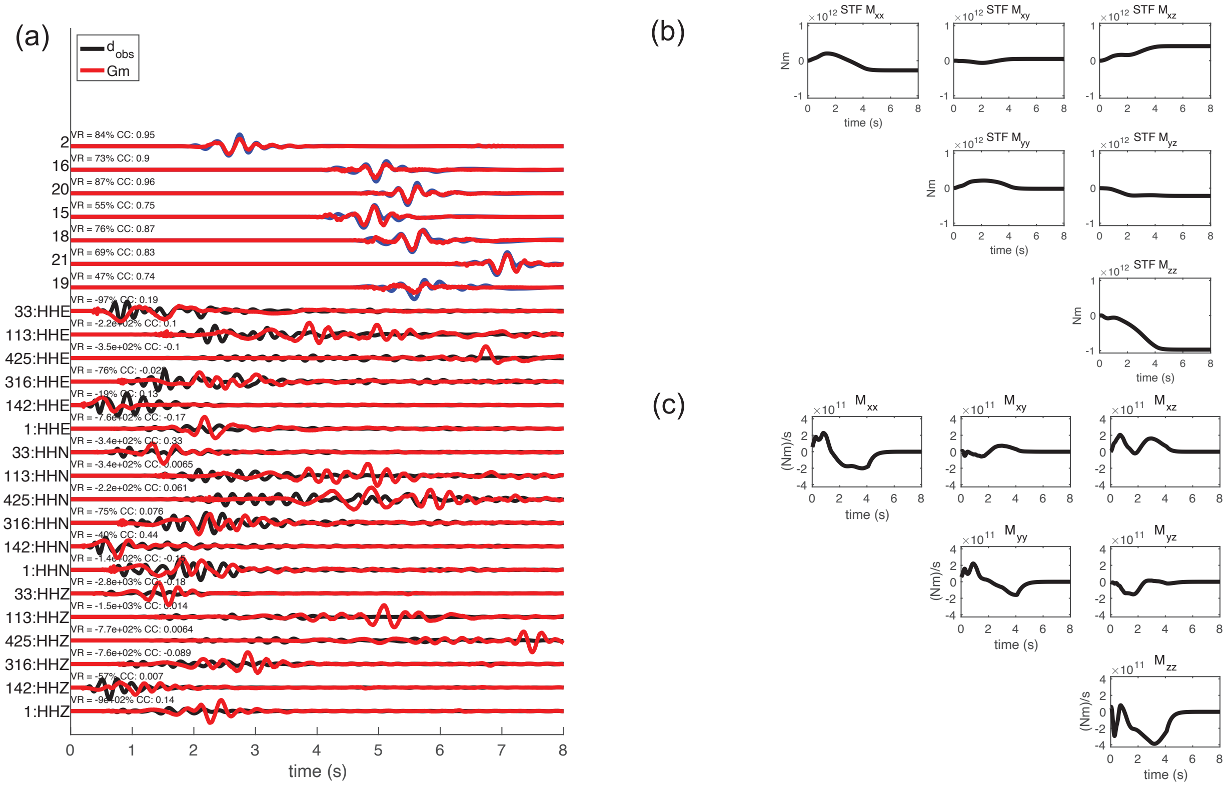

Figure 3-6 (a) Observed seismic (black) and acoustic (blue) compared to predicted (red) data from inversion of seismic and acoustic signals. (b) Estimated source-time moment functions of the buried seismic source. (c) Source-time moment rate functions of the buried seismic source, which are directly estimated in the inversion.

Adding in the vertical spall term, Fz, again slightly increases the data fit (see Figure 3-7a), following what we observed from the infrasound-only inversions for each station, but the overall quality of the fit remains quite low for the seismic data. Additionally, the Fz terms for both of these seismoacoustic inversions are highly oscillatory, unlike the results from the infrasound inversions and again, as in the infrasound inversions, the seismoacoustic inversions that include Fz are highly unstable.

These low data misfits suggest that we cannot accurately resolve both the seismic and acoustic signals with the current inversion scheme.

Lastly, we portray our seismoacoustic inversion results on fundamental lunes (Figure 3-8) so as to estimate the overall trends of the moment tensor results, although we again acknowledge that due to the data fits, these lunes are likely incorrect or at best oversimplified. Unlike in the acoustic results, the seismoacoustic results have very similar starts, focused around an explosion. Both results then contain linear vector dipole and double-couple contributions to the data. Similar to the acoustic-only results, the estimated isotropic STFs do not follow the typical trend for an explosive source.

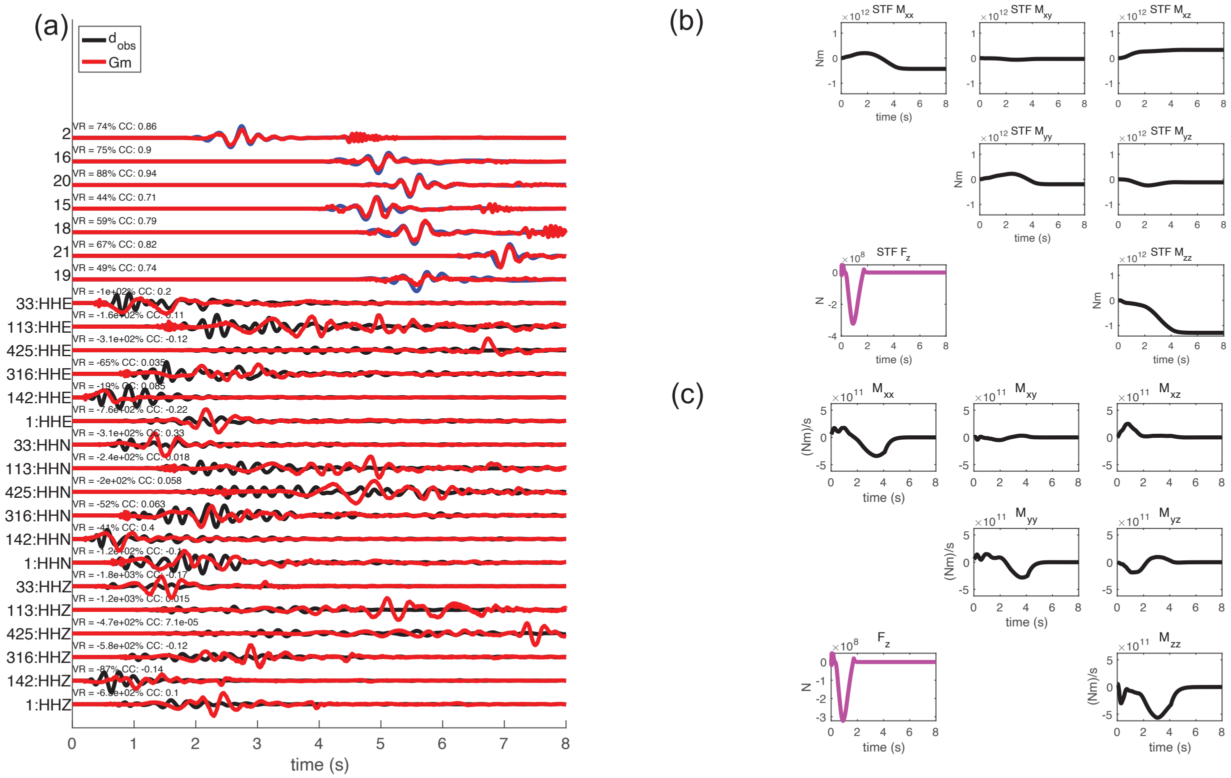

Figure 3-7 Similar to Figure 3-6, except that our inversion estimates both buried seismic source (Mij) and spallation (Fz) source-time moment rate functions.

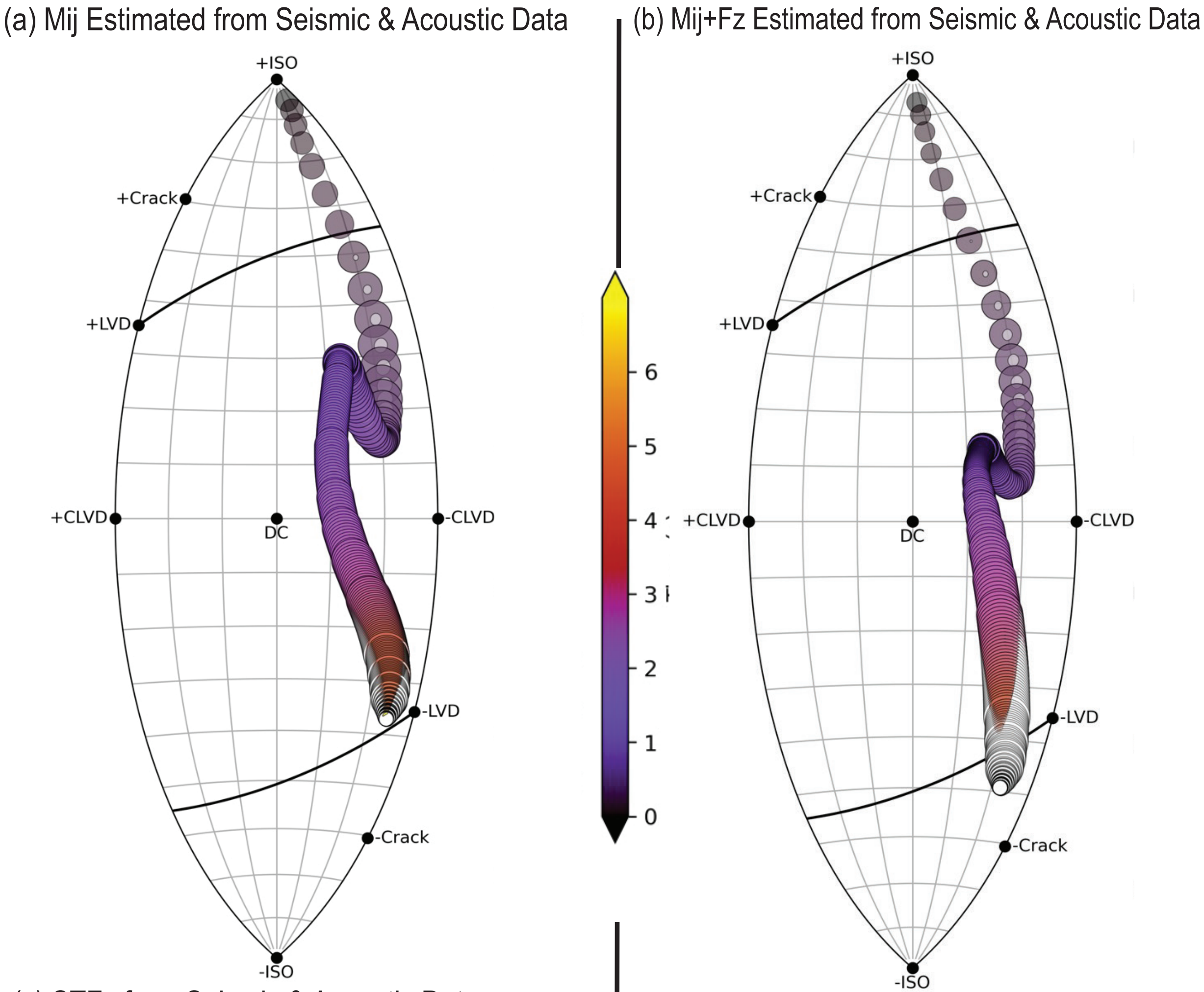
(a) Mij Estimated from Seismic & Acoustic Data

(b) Mij+Fz Estimated from Seismic & Acoustic Data

(c) STFs from Seismic & Acoustic Data

(d) STFs from Seismic & Acoustic Data

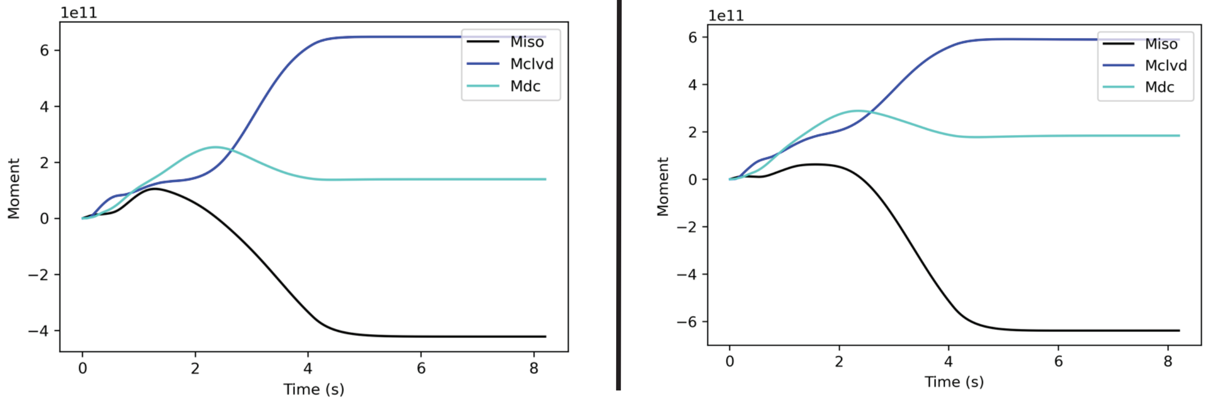

Figure 3-8 Lune visualization of the estimated buried source moment rate functions using (a) seismic and acoustic data to resolve Mij alone as compared to (b) seismic and acoustic signals to resolve Mij and Fz STFs. (c) Decomposition of Mij in terms of compensated linear vector dipole (CLVD), double couple (DC), and isotropic (ISO) STFs. (d) Similar to (c), but for Mij when Fz is incorporated into the inversion.

4. DISCUSSION

Our exploration into the limitations and capabilities of acoustic data in representing the time-variable moment tensor of a buried source has led to several key findings. The initial Mij inversion highlighted a fundamental challenge: acoustic data alone faces significant difficulties in constraining a physically realistic depiction of the buried source's moment tensor over time (Figure 3-2 and Figure 3-5a). This limitation underscores the inherent complexities in capturing the dynamic behavior of such sources through acoustic measurements alone.

Introducing the spallation term (Mij+Fz) into our analysis marked a pivotal advancement (see Figure 3-3). We observed an initial explosion phase that rapidly transitioned into double couple and CLVD components (see Figure 3-5b). This modification brought a more realistic portrayal of the buried source term, with the spallation term's positive nature—indicative of an upward motion—successfully capturing the initial upheaval phase. This phase is a critical contributor to the acoustic signal, aligning with our expectations of the spallation source's behavior. However, it's important to note that for both Mij and Mij+Fz results, the final isotropic component of the source time function, in terms of moment, deviated from the expected characteristics of an explosion (see Figure 3-5). This deviation signals a need for further refinement in our modeling approach to more accurately represent the source dynamics.

When our focus shifted to solely determining Fz from the acoustic data, we achieved a fit to the acoustic data (Figure 3-4) with nearly the same accuracy as when incorporating more source terms. This finding is consistent with previous work, suggesting that acoustic data is most sensitive to the spallation and ground upheaval from the buried source, rather than the buried source itself. This sensitivity highlights the potential of acoustic data to capture specific aspects of the source dynamics, particularly those related to the spallation and upheaval phenomena.

The integration of seismic data through a joint inversion to resolve the buried source introduced a significant improvement in the realism of the time-variable moment tensor's evolution (Figure 3-5). However, similar to our earlier findings, the final isotropic component of the source time function, in terms of moment, again deviated from the typical characteristics of an explosion. This consistent deviation across different modeling approaches underscores the complexity of accurately capturing the isotropic component of the source dynamics and suggests a need for alternative methods. Future work should focus on investigating new ways to jointly invert seismic and infrasound datasets. These methods should aim to better fit the disparate datasets and balance the contributions from both seismic and infrasound data effectively. Expanding the infrasound data and Green's Functions to include local infrasound could offer a more nuanced understanding of the buried source. This local infrasound signal is captured by the the Hyperion sensors, illustrated in Figure 2-1, and may provide additional sensitivity to the buried source beyond what primary acoustic signals can offer.

5. CONCLUSION

In this study, we conducted inversions of infrasound and seismoacoustic data to estimate the time-variable buried seismic source components as well as the vertical surface spall source, Fz, in terms of moment rate. We explored how varying the number of resolved source terms affects the ability of the inversion to resolve the changing nature of the DAG-4 source mechanism through time using infrasound data alone. Additionally, we created a seismoacoustic joint inversion formulation that had difficulty fitting the observed infrasound and seismic data. Future work will involve exploring the estimates of coupling in our source model, improving the Green's functions used, and improving the joint inversion framework by trying other joint inversion techniques such as a sequential approach.

REFERENCES

Aki, K. and Richards, P. G. (2002). *Quantitative seismology*. University Science Books, 2 edition.

Baker, G. E., Stevens, J. L., and Xu, H. (2012a). Explosion shear-wave generation in high-velocity source media. *Bulletin of the Seismological Society of America*, 102(4):1301–1319.

Baker, G. E., Stevens, J. L., and Xu, H. (2012b). Explosion shear-wave generation in low-velocity source media. *Bulletin of the Seismological Society of America*, 102(4):1320–1334. _eprint: https://pubs.geoscienceworld.org/ssa/bssa/article-pdf/102/4/1320/2664717/1320.pdf.

Berg, E. and Poppeliers, C. (2022a). Unraveling the Wrinkle in Time-Variable Sources with Lunes and Synthetic Seismic Data. Technical Report SAND2022-13242, Sandia National Lab. (SNL-NM), Albuquerque, NM (United States).

Berg, E. M. and Poppeliers, C. (2022b). Inversion of Infrasound Time Series for Seismoacoustic Source Parameters Produced by a Buried Chemical Explosion at the Source Physics Experiment Phase II: Dry Alluvium Geology. *Bulletin of the Seismological Society of America*, 112(4):2216–2230.

Chiang, A., Dreger, D. S., Ford, S. R., Walter, W. R., and Yoo, S.-H. (2016). Moment tensor analysis of very shallow sources. *Bulletin of the Seismological Society of America*, 106(6). Institution: Lawrence Livermore National Lab. (LLNL), Livermore, CA (United States) Number: LLNL-JRNL-718465 Publisher: Seismological Society of America.

Day, S. M., Cherry, J. T., Rimer, N., and Stevens, J. L. (1987). Nonlinear model of tectonic release from underground explosions. *Bulletin of the Seismological Society of America*, 77(3):996–1016. Publisher: GeoScienceWorld.

Day, S. M. and McLaughlin, K. L. (1991). Seismic source representations for spall. *Bulletin of the Seismological Society of America*, 81(1):191–201.

Day, S. M., Rimer, N., and Cherry, J. T. (1983). Surface waves from underground explosions with spall: Analysis of elastic and nonlinear source models. *Bulletin of the Seismological Society of America*, 73(1):247–264.

Ford, S. R., Dreger, D. S., and Walter, W. R. (2009). Source analysis of the Memorial Day explosion, Kimchaek, North Korea. *Geophysical Research Letters*, 36(21). _eprint: https://onlinelibrary.wiley.com/doi/pdf/10.1029/2009GL040003.

Haskell, N. A. (1967). Analytic approximation for the elastic radiation from a contained underground explosion. *Journal of Geophysical Research (1896-1977)*, 72(10):2583–2587.

Herrmann, R. B., Benz, H., and Ammon, C. J. (2011). Monitoring the Earthquake Source Process in North America. *Bulletin of the Seismological Society of America*, 101(6):2609–2625.

Hudson, J. A., Pearce, R. G., and Rogers, R. M. (1989). Source type plot for inversion of the moment tensor. *Journal of Geophysical Research: Solid Earth*, 94(B1):765–774.

Kisslinger, C., Mateker Jr., E. J., and McEvilly, T. V. (1961). SH motion from explosions in soil. *Journal of Geophysical Research (1896-1977)*, 66(10):3487–3496. _eprint: https://onlinelibrary.wiley.com/doi/pdf/10.1029/JZ066i010p03487.

Patton, H. J. and Taylor, S. R. (1995). Analysis of lg spectral ratios from NTS explosions: Implications for the source mechanisms of spall and the generation of lg waves. *Bulletin of the Seismological Society of America*, 85(1):220–236.

Poppeliers, C., Anderson Aur, K., and Preston, L. (2018). The Relative Importance of Assumed Infrasound Source Terms and Effects of Atmospheric Models on the Linear Inversion of Infrasound Time Series at the Source Physics Experiment. *Bulletin of the Seismological Society of America*, 109(1):463–475.

Poppeliers, C. and Preston, L. (2020). Inverting infrasound data for the seismoacoustic source time functions and surface spall at the Source Physics Experiments Phase II: Dry Alluvium Geology. Technical Report SAND-2020-9217, Sandia National Lab. (SNL-NM), Albuquerque, NM (United States).

Poppeliers, C. and Preston, L. (2021). The effects of earth model uncertainty on the inversion of seismic data for seismic source functions. *Geophysical Journal International*, 224(1):100–120.

Poppeliers, C. and Preston, L. (2022a). Combining translational and rotational seismic motions to invert local-scale seismic data for time-variable moment tensors: do rotational motions help for high-frequency seismic data produced by underground explosions? *Geophysical Journal International*, 230(1):235–251.

Poppeliers, C. and Preston, L. (2022b). An efficient method to propagate model uncertainty when inverting seismic data for time domain seismic moment tensors. *Geophysical Journal International*, 231(2):1221–1232.

Prothro, L. B. and Wagoner, J. (2020). Geologic framework model for the Dry Alluvium Geology (DAG) experiment testbed, Yucca Flat, Nevada National Security Site. Technical Report DOE/NV/03624-0878, Nevada National Security Site/Mission Support and Test Services LLC (NNSS/MSTS), North Las Vegas, NV (United States).

Rösler, B. and Stein, S. (2022). Consistency of Non-Double-Couple Components of Seismic Moment Tensors with Earthquake Magnitude and Mechanism. *Seismological Research Letters*, 93(3):1510–1523.

Stevens, J. L., Baker, G. E., Xu, H., Bennett, T. J., Rimer, N., and Day, S. D. (2004). The physical basis of lg generation by explosion sources. *LLNL Technical Report*.

Stevens, J. L. and Thompson, T. W. (2015). 3D Numerical Modeling of Tectonic Strain Release from Explosions. *Bulletin of the Seismological Society of America*, 105(2A):612–621.

Tape, W. and Tape, C. (2012). A geometric setting for moment tensors. *Geophysical Journal International*, 190(1):476–498.

Tape, W. and Tape, C. (2013). The classical model for moment tensors. *Geophysical Journal International*, 195(3):1701–1720.

Vieceli, R. E., Abbott, R. E., and Preston, L. A. (2022). Assessing the Accuracy of a Borehole-Controlled P-Wave Velocity Model of Yucca Flat, Nevada Using Large-N Seismic Data. *Bulletin of the Seismological Society of America*, 112(3):1373–1383.

Wallace, T. C., Helmberger, D. V., and Engen, G. R. (1983). Evidence of tectonic release from underground nuclear explosions in long-period P waves. *Bulletin of the Seismological Society of America*, 73(2):593–613.

Wright, J. K. and Carpenter, E. W. (1962). The generation of horizontally polarized shear waves by underground explosions. *Journal of Geophysical Research (1896-1977)*, 67(5):1957–1963. _eprint: https://onlinelibrary.wiley.com/doi/pdf/10.1029/JZ067i005p01957.

DISTRIBUTION

Email—Internal

Name	Org.	Sandia Email Address
Elizabeth Berg	6756	eliberg@sandia.gov
Andréa Darrh	8911	adarrh@sandia.gov
Leiph Preston	8911	lpresto@sandia.gov
Marlon Ramos	6756	mdramos@sandia.gov
Technical Library	1911	sanddocs@sandia.gov

Email—External

Name	Company Email Address	Company Name
Rengin Gok	m.rengin.gok@nnsa.doe.gov	NNSA
John Lazarz	john.lazarz@nnsa.doe.gov	NNSA
Christian Poppeliers	christian.poppeliers.ctr@us.af.mil	Leidos, Air Force Technical Applications Center

Hardcopy—Internal

Number of Copies	Name	Org.	Mailstop
1	None	-	-

Hardcopy—External

Number of Copies	Name(s)	Company Name and Company Mailing Address
1	None	-

Sandia National Laboratories